Energy Advances

ROYAL SOCIETY OF CHEMISTRY

PAPER

View Article Online
View Journal | View Issue

Check for updates

Cite this: *Energy Adv.*, 2026, 5, 538

Deciphering solid–electrolyte interface in cellulose-montmorillonite nanocomposites for sodium batteries

Sneha Mandal,[a] Catherine Tom,[b] Subbiah Alwarappan,[c] Ravi Kumar Pujala,[b] Surendra K. Martha[d] and Vijayamohanan K. Pillai*[a]

Received 19th January 2026,
Accepted 22nd February 2026

DOI: 10.1039/d6ya00014b

rsc.li/energy-advances

Electrolytes and their interphases are critical for emerging battery chemistries such as metal–sulphur and metal–oxygen, especially in the case of solid electrolytes, which offer attractive energy storage possibilities but involve drastic phase transitions and structural challenges. Therefore, developing improved electrolytes and interphases is a key to achieving sustainable battery performance. Here, we introduce a novel polymer composite electrolyte utilising abundant montmorillonite and cellulose nanocrystals (CNC), creating a stable interphase with the Na metal and alleviating common degradation issues. For example, this electrolyte exhibits a stability window of 2.3–5.3 V and a transference number of ~0.87, although its durability and performance need further improvement. FT-IR spectroscopy, XPS, and Raman spectroscopy provide valuable insights into the interfacial chemistry, as evidenced by a prominent hydroxyl stretching band associated with the CNC. While hydroxyl groups may compromise interfacial stability at the cathode, possibly causing cell degradation, they simultaneously enhance the sodium-ion mobility at the anode by facilitating favourable coordination with sodium metal. This dual function underscores the need for tuning functional groups in electrolyte design.

Open Access Article. Published on 06 March 2026. Downloaded on 6/16/2026 1:20:17 PM.
This article is licensed under a Creative Commons Attribution-NonCommercial 3.0 Unported Licence.

1. Introduction

Recent incidents involving battery explosions highlight the critical importance of prioritizing safety in designing and deploying energy storage technologies. Solid-state batteries (SSBs), with their inherently safer design and non-flammable electrolytes, have the potential to significantly reduce the risk of such hazardous incidents.[1–3] The electrolyte, a central component in battery chemistry, is vital as it physically interacts with many other battery components. For example, it facilitates the movement of ions, effectively insulates electrons, and maintains stability when exposed to active materials of both highly reductive cathodes and strongly oxidative anodes. As a result, the mechanical, electrical, and chemical properties of the solid electrolyte have a critical impact on the safety and influence of various physicochemical processes within the cell. This, in turn, can lead to a greater stability of the electrochemical system, especially when coupled with high-energy anodes such as Li, Na, and Si.[4–6] In this context, the use of composite polymer electrolytes with robust microscopic structures and non-flammability significantly improves operational safety, with some tolerance to overcharge/deep discharge. Moreover, solid inorganic electrolytes (SIEs) are often single-ion conductors, which leads to higher charge-transport efficiencies (10^{-3} S cm^{-1}) than traditional liquid electrolytes, with lower transference numbers (≤ 0.5). However, SIEs are brittle in nature, and maintaining good contact over a prolonged cycle life is difficult. Furthermore, they undergo volume changes, and a constant pressure needs to be maintained for proper contact, as elegantly demonstrated recently.[7–10]

The use of two-dimensional materials with large surface areas, high doping propensity, facile surface modification, and compatibility with layer-by-layer fabrication boosts ionic transport and promotes the thermal and mechanical stability of solid–polymer electrolytes, especially after composite formation.[11–13] Recently, two-dimensional (2D) boron nitride (BN) nanosheets, graphene oxides, and MXenes have been widely adopted as fillers and additives to enhance the ionic conductivity and mechanical strength of polymer electrolytes. However, the instability and poor processability of these nanomaterials remain the main limitations for their widespread application.[14–16] In this context, clay materials have

[a] *Department of Chemistry, Indian Institute of Science Education and Research (IISER), Tirupati-517619, India. E-mail: vijay@iisertirupati.ac.in*
[b] *Department of Physics, Indian Institute of Science Education and Research (IISER), Tirupati-517619, India*
[c] *Electrodics and Electrocatalysis Division, CSIR-Central Electrochemical Research Institute, Karaikudi-630003, Tamil Nadu, India*
[d] *Department of Chemistry, Indian Institute of Technology (IIT), Hyderabad-502285, India*

© 2026 The Author(s). Published by the Royal Society of Chemistry

Open Access Article. Published on 06 March 2026. Downloaded on 6/16/2026 1:20:17 PM. This article is licensed under a Creative Commons Attribution-NonCommercial 3.0 Unported Licence.

emerged as attractive alternatives for hydrogels and semi-solid electrolytes owing to their large specific surface area, distinct physical and chemical adsorption properties, environmental friendliness, and cost-effectiveness.[17,18] Among these, aluminium magnesium silicate (montmorillonite or MMT) has drawn considerable research interest in battery applications. Its layered structure, featuring octahedral sheets sandwiched between two silica tetrahedral sheets, endows it with excellent chemical stability, robust mechanical properties, and environmental compatibility. Many of the above limitations could be alleviated by a composite polymer electrolyte using a suitable polymer matrix such as cellulose; hence, unsurprisingly, several recent results using MMT in various energy storage systems have shown promising outcomes.[19–21] For instance, He *et al.* synthesised a gel polymer electrolyte based on a polyacrylonitrile/organic montmorillonite membrane, which served as a host for $LiPF_6$ in ethylene carbonate.[22] Similarly, Kim *et al.* prepared a polymer composite electrolyte with PEO and $LiClO_4$ with different percentages of Li–MMT as a filler.[23] Zhao *et al.* synthesised a solid composite electrolyte based on a PEO matrix with LiTFSI and LLZTO in acetonitrile and MMT as a filler.[24] Dhatarwal *et al.* used a solution-cast method to prepare nanocomposite solid polymer electrolyte (NSPE) films incorporating MMT clay nanoplatelets based on a poly(ethylene oxide) and poly(methyl methacrylate) blend matrix with lithium tetrafluoroborate ($LiBF_4$).[25] In comparison, Chen *et al.* prepared a montmorillonite composite poly(ether sulfone) ion-conducting membrane (MMT-M) where MMT, with high mechanical strength and negative charge, was used as a functional coating compounded on the matrix (PS-M) consisting of poly(ether sulfone) and sulfonated poly(ether ketone) for a zinc–iron flow battery.[26] However, in these studies, montmorillonite was used as a filler either to change the domain size or to increase the mechanical strength and thermal stability. None of the previous works has investigated MMT as a candidate for polymer composite electrolytes containing free mobile Na^+ ions within the interlayer. Also, the proposed electrolyte is flexible; thus, the application of pressure is not required, and it exhibits room temperature conductivity in the order of 10^{-5}–10^{-6} S cm^{-1}, unlike its ceramic oxide counterpart. These features make MMT a promising candidate for sodium-based energy storage devices.

Accordingly, we recently reported clay–nanocellulose composite polymer electrolytes in which tuning the domain size and correlating structure–property relationships led to enhanced ionic conductivity.[27] In a subsequent study on LAPONITE®-nanocellulose composite polymer electrolytes, we showed that hydroxyl groups interfere (1.5% concentration increase) at the cathode–electrolyte interface, resulting in interfacial instability and capacity fading during cycling.[28] However, several questions related to the interfacial stability were elusive, including the precise role of hydroxyl functionalities in governing cathode–electrolyte interfacial chemistry, the dual role of the hydroxy groups, and degradation analysis of the coin cells coupled with the MoS_2 electrode during cycling. In a continuation, here we demonstrate the electrochemical properties and solid–electrolyte interface issues, utilising MMT and CNCs to fabricate free-standing polymer nanocomposite films. The negatively charged CNC rods interact non-covalently with the positively charged edges of the MMT clay to presumably form a gel, as indicated by the zeta potential measurements.[27] The free-standing films of CNC/MMT composite, fabricated through the evaporation-induced self-assembly process, exhibit complex ordered structures, which can boost the sodium ion transport through their ordered network. These films have a wide electrochemical stability window of 2.3–5.3 V, and a high transference number of 0.87, facilitating their usage as a battery electrolyte. The as-prepared electrolyte has been coupled with MoS_2 free-standing sheets as cathodes and Na metal as anodes for the fabrication of Na cells.

2. Materials and methods

Few-layer MoS_2 nanosheets were prepared using the liquid-phase exfoliation method. Typically, bulk MoS_2 (3 g) (Sigma Aldrich) was stirred with *n*-butyl lithium in 1.5 M hexane (25 mL) (SRL) for 48 h under argon. The black slurry obtained was vacuum-filtered with hexane, and the dried powder was further dispersed in water and sonicated for 1 h for exfoliation. Lastly, the dispersed MoS_2 was centrifuged to obtain a few layers of exfoliated MoS_2 ($\sim$2.5 g). A typical electrode slurry was prepared using 85% MoS_2, 5% PEDOT-PSS, and 10% CNC, which was coated onto a polyvinyl acrylate sheet with a uniform thickness using a doctor-blade. To obtain the free-standing films, the prepared composite films were immersed in acetone. Free-standing composite polymer electrolyte thin films with a composition of 2.5C:1M (C-CNC; M-MMT) were prepared by the casting method, as discussed elsewhere.[27]

2.1 Material characterization

FTIR analysis for the CNC–MMT polymer composites and MoS_2 electrodes was carried out in the 450 to 4000 cm^{-1} range with a resolution of 2 cm^{-1}, using a PerkinElmer ATR C117460 instrument. Raman analysis was performed with a confocal and resonance Raman instrument (LabRam, Horiba Scientific) with a spatial resolution of 1 μm, by placing the samples on top of quartz slides; a 40 mW, 405 nm excitation laser was used. X-ray photoelectron spectroscopy (XPS) measurements were performed with a Thermo Scientific–ESCALAB 250 xi instrument. Field-emission gun transmission electron microscope (FEG-TEM) images were acquired with a JEOL JEM-2100F instrument to observe a lattice resolution of 0.1 nm and point-to-point resolution of 0.19 nm with 200 kV acceleration voltage. Powder X-ray diffraction of the samples was recorded with a Smart Lab 9 kW Rigaku using a monochromatic Cu Kα source (λ = 1.5406 Å) at 45 kV and 200 mA.

2.2 Electrochemical characterisation

12 mm electrodes and 18 mm electrolyte discs were dissected using a cutter, followed by vacuum-drying at 70 °C, before fabricating the CR2032 cells inside an Ar-filled glove box. A

Open Access Article. Published on 06 March 2026. Downloaded on 6/16/2026 1:20:17 PM.
This article is licensed under a Creative Commons Attribution-NonCommercial 3.0 Unported Licence.

battery tester BCS 805 (Biologic, France) was used to measure galvanostatic charge/discharge, and linear sweep voltammetric studies of the MoS_2 electrode were carried out using the composite electrolyte. Electrochemical impedance studies were performed for the electrolyte at an open-circuit voltage using an AC amplitude of 5 mV (RMS value) in the range of 1 MHz–0.1 Hz with a Solartron 1470E electrochemical workstation. The electrochemical stability window of the 2.5C:1M thin film was investigated using linear sweep voltammetry (LSV). By placing the thin film between a stainless-steel working electrode and a metallic sodium counter (reference) electrode at a scan rate of 0.1 mV s^{-1} between 2.3 to 6 V. For chronoamperometry measurements, a similar thin film of the composition 2.5C:1M was sandwiched between two freshly prepared Na–metal discs, and the current–time response was measured under a constant DC bias of 10 mV. The reversible ion transport through the 2.5C:1M thin film and the sodium electrodeposition behaviour were studied using galvanostatic cycling in a symmetric (Na/Na) cell configuration at room temperature by probing the reversible voltage response under a constant current density of $\pm$0.1 mA cm^{-2} for a sodium plating/stripping capacity of 0.1 mA h cm^{-2}.

3. Results

The schematic in Scheme 1 illustrates that the hydroxy functional groups on CNC promote the formation of a stable anode–electrolyte interface with sodium metal, enhancing interfacial stability. In contrast, at the cathode side, these hydroxy groups interfere with solid–electrolyte interface (SEI) formation, leading to a heterogeneous and unstable cathode–electrolyte interface.

In order to gain insights into the structural changes in CNC–MMT composites and MoS_2 after exfoliation, we performed XRD and Raman spectroscopy to study the systematic changes in *d*-spacing. Accordingly, Fig. 1(a) and (b) present the XRD patterns of the CNC–MMT composite and MoS_2 nanosheets, respectively. In the CNC–MMT composite, the characteristic (001) plane exhibits an interesting shift in 2θ from 7.2° to 6.1°, corresponding to an increase in *d*-spacing of 2.08 Å, which reveals that the one-dimensional (1D) CNC was successfully intercalated into the two-dimensional (2D) MMT nanosheets.[29,30] This was further observed from the cross-sectional SEM and small-angle X-ray scattering (SAXS) measurements.[27] Furthermore, while broadening is observed in CNC and MMT diffraction peaks, no significant changes in peak asymmetries occur, since the stacking disorder is perhaps negligible, preserving the integrity of the layered structure of the Montmorillonite. Similarly, the XRD pattern of the MoS_2 nanosheets (Fig. 1(b)) reveals a broadening of the (002) peak after exfoliation compared with that of the pristine sample, indicating the stacking of the 2D nanosheets along the *z*-direction. Interestingly, the (002) peak shifts to a lower angle, while the (100) peak shifts to a higher angle, suggesting an expansion along the (001) direction and in-plane compression in the synthesized MoS_2 nanosheets (6.15 Å). Additionally, a new (001) peak at $2\theta \approx 6.4°$ corresponds to a layer separation of approximately 5.5–6 Å during restacking, indicating the formation of the 1T phase. The broadness of the (002) peak and the presence of the (001) peak suggest that the nanosheets are randomly arranged during restacking, with a significant expansion of the interlayer spacing.[31,32]

Fig. 1c compares the Raman spectra for the pristine and exfoliated MoS_2 nanosheets. The spectra reveal the characteristic E^1_{2g} and A_{1g} bands at 377 and 402 cm^{-1}, respectively, for pristine MoS_2, corresponding to the in-plane and out-of-plane vibrations of sulphur atoms relative to molybdenum atoms. Furthermore, the exfoliated MoS_2 exhibits a peak at $\sim$222 cm^{-1} corresponding to the J_2 phonon mode, characteristic of metallic 1T-MoS_2, which contributes to forming a super-lattice structure,[33,34] although the J_1 band is missing, as these are excitation-dependent. The exfoliated nanosheets exhibit a blue

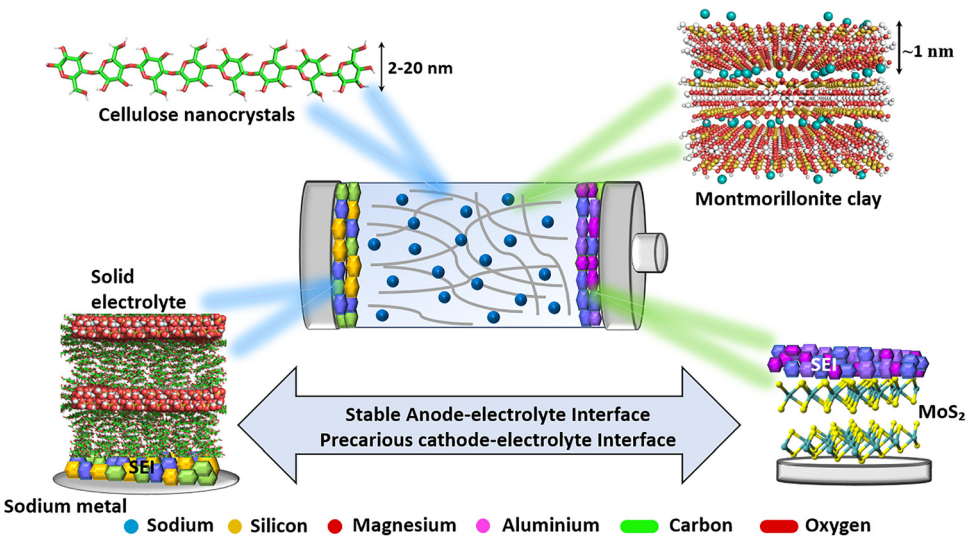

Scheme 1 Illustration of the formation of the solid–electrolyte interface on the anode and cathode.

© 2026 The Author(s). Published by the Royal Society of Chemistry

Open Access Article. Published on 06 March 2026. Downloaded on 6/16/2026 1:20:17 PM.
This article is licensed under a Creative Commons Attribution-NonCommercial 3.0 Unported Licence.

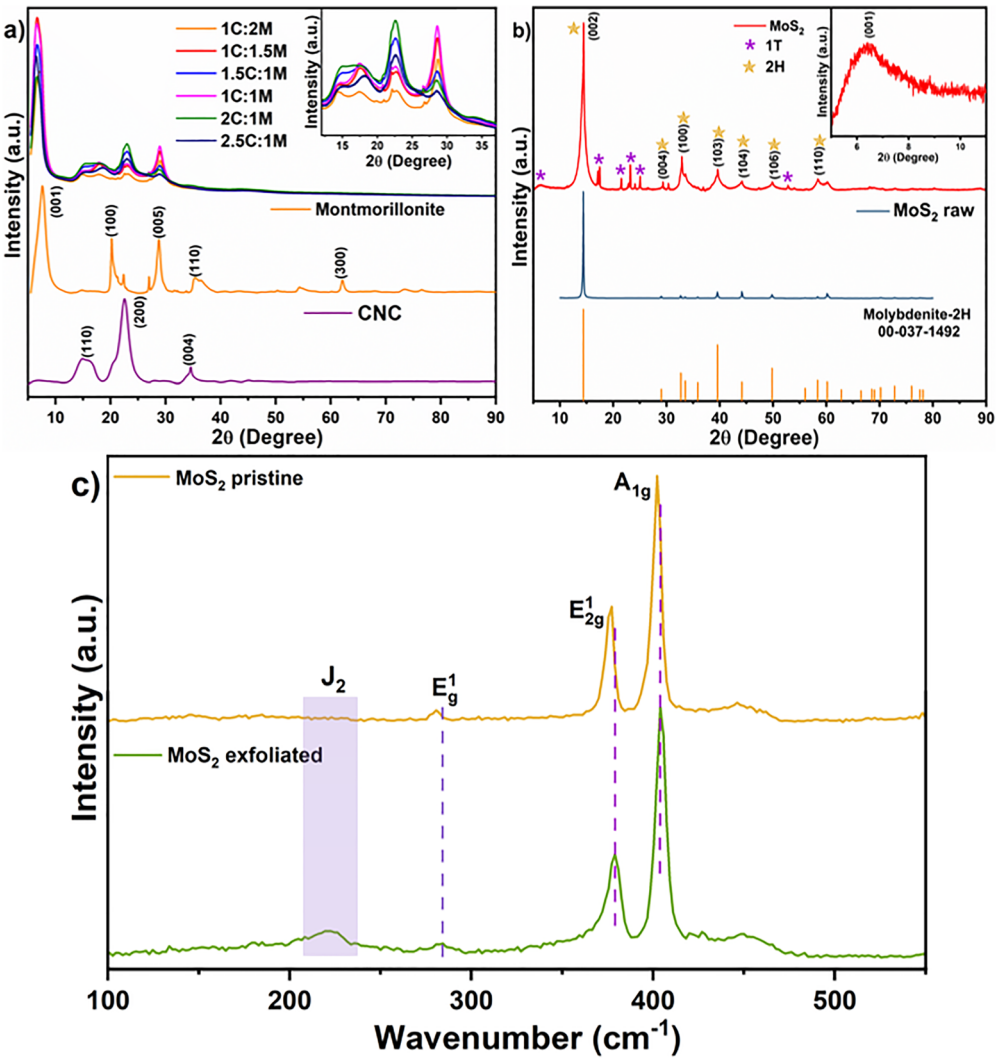

Fig. 1 (a) X-ray diffractograms of CNC–MMT composite electrolytes and (b) comparative diffractograms of pristine and exfoliated MoS_2 nanosheets. (c) Comparative Raman spectra of pristine and exfoliated MoS_2 nanosheets (C and M indicate CNC and MMT, respectively).

shift to 379 and 403 cm^{-1} for these bands, while the intensity ratio (I_E/I_A) for pristine and exfoliated samples is 0.46 and 0.4, respectively, suggesting that the particle size remains mostly unchanged after exfoliation.[35,36] The frequency, intensity, and width of the E^1_{2g} and A_{1g} bands are influenced by the thickness (layer count) of the MoS_2 flakes. Many studies indicate that exfoliation typically narrows the separation between these bands, with a common shift to 381 cm^{-1} for E^1_{2g} and 406 cm^{-1} for A_{1g}. However, some research demonstrates that, depending on the quality of the bulk MoS_2, broad peaks for E^1_{2g} and A_{1g} can appear at 375 and 402 cm^{-1}, respectively.[37,38] Interestingly, in such cases, exfoliation leads to a blue shift for both bands to 381 cm^{-1} (E^1_{2g}) and 405 cm^{-1} (A_{1g}), rather than reducing their separation. This study also identifies a similar blue shift. Instead of diminishing the band separation, the E^1_{2g} and A_{1g} modes shift to higher wave numbers. Nevertheless, the shift in the A_{1g} band is less pronounced compared with the E^1_{2g} band, yielding a band separation of 24 cm^{-1} *versus* 26 cm^{-1} in bulk MoS_2. This shift may stem from lattice strain effects induced in MoS_2 nanosheets by interactions with *n*-butyl lithium (*n*-butyl Li), as Yang *et al.*[39] describe, or from defects developed during exfoliation. This interaction causes greater in-plane strain than out-of-plane strain, consistent with Raman spectra showing similar shifts in the E^1_{2g} and A_{1g} bands under in-plane lattice strain.

The deconvoluted Mo 3d spectrum of free-standing 2H-MoS_2 shows two prominent peaks at 232.3 and 229.1 eV, corresponding to Mo^{4+} $3d_{3/2}$ and Mo^{4+} $3d_{5/2}$, respectively, while the exfoliated nanosheets show peaks at 232.18 and 229.02 eV, respectively, with a shift of 0.12 and 0.19 eV. The S $2p_{3/2}$ and $2p_{1/2}$ peaks of MoS_2 exhibit similar downshifts (Fig. 2b and d) as a result of the presence of the metallic 1T phase. It has been observed that the components from the 1T phase appear at a binding energy that is ~0.9 eV lower than their 2H counterparts. The prominent peaks at ~233 and 235 eV show oxidation of Mo, corresponding to Mo^{6+}. Similarly, for S 2p,

Open Access Article. Published on 06 March 2026. Downloaded on 6/16/2026 1:20:17 PM.
This article is licensed under a Creative Commons Attribution-NonCommercial 3.0 Unported Licence.

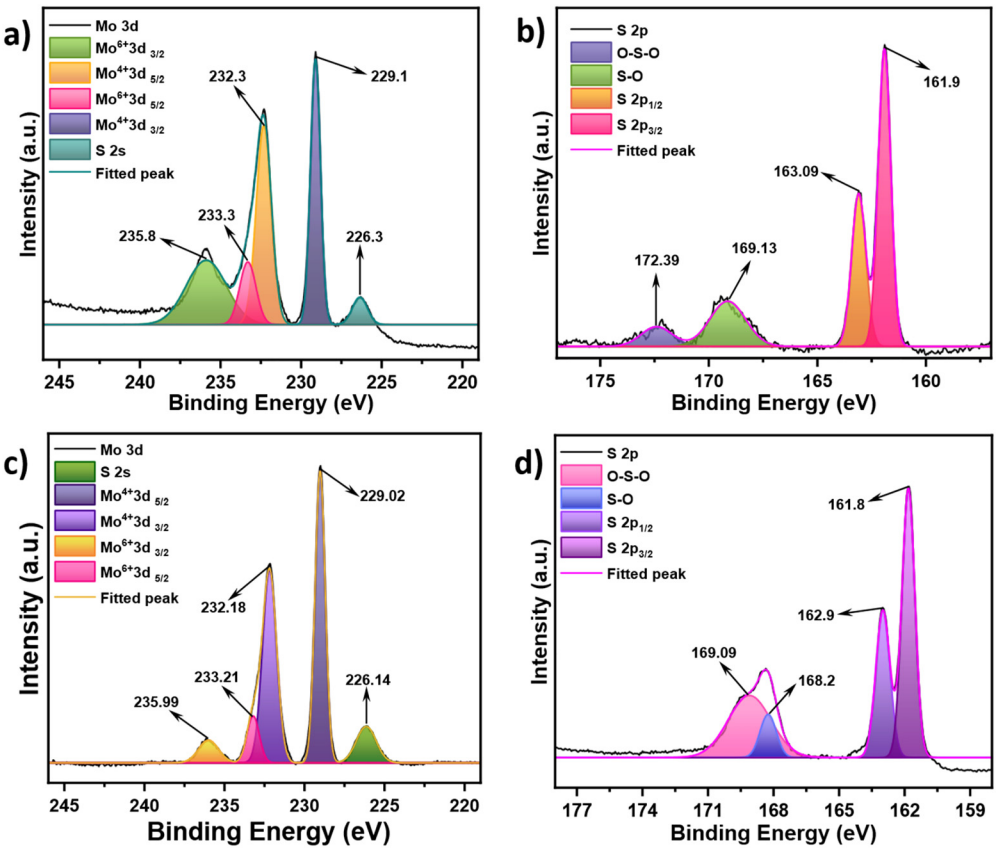

Fig. 2 X-ray photoelectron spectra (XPS) of (a) and (b) free-standing MoS_2 (Mo: 12 meV and S: 19 meV shift) and (c) and (d) exfoliated MoS_2 film.

peaks observed between 168 and 170 eV, after exfoliation, indicate that sulphur atoms might have oxidized or the shift is due to the interaction with PEDOT/PSS.[40–42]

The deconvoluted post-cycling Mo 3d spectrum (Fig. S1a) reveals an interesting shift in the peaks, providing valuable insights into the electronic interactions possible during cycling. For example, two prominent peaks at 228.8 and 231.2 eV correspond to Mo^{4+} $3d_{5/2}$ and Mo^{4+} $3d_{3/2}$, respectively. Additionally, a MoO_3 peak appears at 233.9, indicating that some MoS_2 was oxidized during the cycling, which is attributed to interfacial reactions and the interference of hydroxyl groups. Moreover, the band separation between $3d_{5/2}$ and $3d_{3/2}$ is 3.2 eV and 2.4 eV before and after cycling, respectively, indicating a significant change in the electronic structure, which could be attributed to the oxidation.[43] Similarly, the S 2p spectrum (Fig. S1b) shows a shift in the peaks and the emergence of satellite peaks. The peak at 168.4 eV corresponds to the S–O_4 bond, while 167.3 eV represents the S–O bond, 165.4 eV is attributed to the Mo–O–S bond, and 161 eV reveals the S^{2-} arising from MoS_2. The deconvoluted O 1s spectra (Fig. S1c) show several peaks corresponding to C–O bonds, mainly linking to the CNC. The peak at 535.6 eV corresponds to the C–O–C bond, 534.6 eV, the C–OH bond, and the peak at 530.7 represents the C═O/Mo–O bond.[44]

These observations collectively confirm that notable chemical and electronic modifications occur in the MoS_2 electrode during cycling, with profound implications for the degradation of the cell. The emergence of Mo^{6+} and oxygenated sulphur species, along with the reduced Mo 3d spin–orbit splitting, clearly indicates partial oxidation of MoS_2 and the formation of mixed Mo–O–S environments. The presence of S–O and SO_4^{2-} species further supports interfacial reactions with the electrolyte or hydroxyl groups. Overall, the XPS analysis demonstrates that cycling induces interfacial oxidation and structural reorganization within the MoS_2 framework, also observed in post-cycling SEM, which may significantly influence its electrochemical behaviour and cell failure.

High-resolution transmission electron microscopy (HR-TEM) analysis on both bulk and exfoliated samples revealed typical 2D sheets consisting of thin nanosheets (Fig. 3). The bright and transparent contrast indicates the typical features shown by thin nanosheet structures, with the exfoliation of bulk MoS_2 into a few monolayers with a *d*-spacing of $\sim$0.42 nm, in agreement with the XRD results shown in Fig. 3d. Also, the selected area electron diffraction (SAED) pattern in the inset shows a hexagonal structure with rings, suggesting that the exfoliated nanosheets retain the crystal structure of MoS_2 with a slight rearrangement in the sheets during re-stacking. These nanosheets are in excellent agreement with the results of previous studies.[45–47]

Fig. S2(a–c) presents comparative SEM images of the pristine 2.5C:1M composite electrolyte and after cycling. The images

© 2026 The Author(s). Published by the Royal Society of Chemistry

Open Access Article. Published on 06 March 2026. Downloaded on 6/16/2026 1:20:17 PM.
This article is licensed under a Creative Commons Attribution-NonCommercial 3.0 Unported Licence.

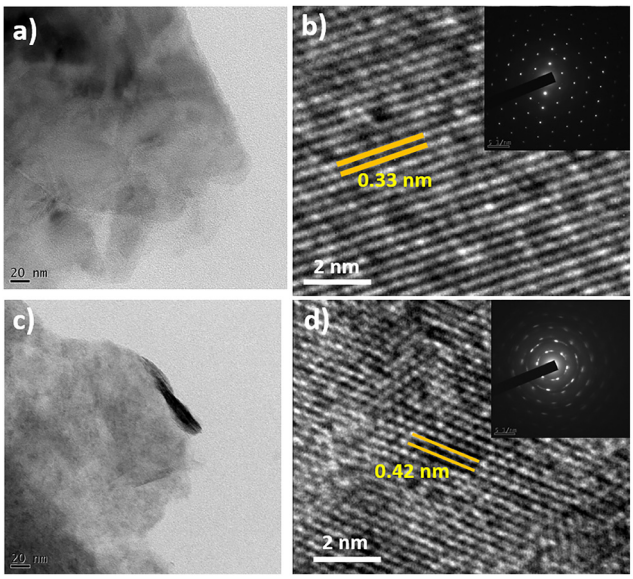

Fig. 3 High-resolution transmission electron microscopic (HR-TEM) images of (a) and (b) pristine MoS_2 nanosheets and (c) and (d) exfoliated MoS_2 nanosheets resulting in an enlarged *d*-spacing of ~0.42 nm (Insets-SAED pattern).

show no visible cracks, suggesting the absence of dendrite formation. Corresponding EDX mapping images for the pristine and post-cycled 2.5C:1M samples (Fig. S3) confirm the uniform distribution of Si, Al, Mg, C, O, and Na throughout the composite polymer electrolyte. Furthermore, as shown in Tables S1 and S2, the oxygen atomic weight percentage increases notably from 33% in the pristine state to 38% after cycling, indicating the formation of hydroxyl groups. Likewise, Fig. S2(d and e) compares the SEM images of pristine and post-cycled MoS_2. The pristine MoS_2 exhibits a sheet-like morphology, while it shows agglomeration post-cycling. EDX mapping (Fig. S4) further confirms the uniform distribution of Mo, S, and O; however, while oxygen is absent in the pristine sample, it appears in the post-cycled MoS_2, highlighting oxygen incorporation at the interface due to hydroxyl groups during cycling.

Various characterisations have been utilised to probe the electrochemical performance of the as-prepared composite polymer electrolyte. For instance, Fig. 4a shows the linear sweep voltammogram (LSV), which is one of the fundamental requirements for analysing the electrochemical stability window for the charge–discharge processes. When the thin film electrolyte is placed between a stainless-steel working electrode and a metallic sodium counter (reference) electrode, the LSV profile spanning 2.3 to 5.5 V suggests robust operational stability. A slight increase in current (in μA) was observed around ~2.7 V, which could be attributed to the oxidation of hydroxy groups or due to a soft short-circuit. With repeated LSV, we did not observe the small peak around ~2.7 V (Fig. S5), and a stability window of ~5.2 V was observed. Fig. S6 shows the Nyquist plot of bare CNC, which shows a conductivity of 1.2×10^{-5} S cm^{-1} compared with that of the composite 2.5C:1M (9.2×10^{-5} S cm^{-1}).[27]

The single-ion conductivity feature of the "as prepared" electrolyte (2.5C:1M) was investigated using chronoamperometry (Fig. 4b). The transference number for the Na^+ ion (t_{Na^+}) was calculated using the well-known Bruce–Vincent method:[48–50]

$$T_+ = \frac{I^s(\Delta V - I^0 R_1^0)}{I^0(\Delta V - I^s R_1^s)}$$

where ΔV is the potential applied across the cell, T_+ is the cationic transference number, R_1^0 and R_1^s are the initial and steady-state resistances of the passivating layers, respectively, and I^0 and I^s are the initial and steady-state currents, 0.48 and 0.36 mA, respectively. The 2.5C:1M composite polymer electrolyte was sandwiched between Na metal discs, and the current–time response was measured under a constant DC bias potential of 10 mV. The measured initial current I^0 reflects the movement of both cations and anions, while the final steady-state current I^s results exclusively from the motion of cations. The slight increase in the resistance ($R_{initial}$ = 200 Ω and R_{ss} = 275 Ω) upon polarization can be explained by the interaction between the ohmic polarization and sodium metal. Based on these results, the t_{Na^+} was calculated to be 0.87.

The initial sharp current spike corresponds to the charging of the electrical double layer at the electrode–electrolyte interface, along with the instantaneous faradaic reaction of electroactive species present directly at the electrode surface. This is followed by a rapid decay in current, which reflects the diffusion-controlled transport of reactants from the bulk solution to the electrode, typically described by the Cottrell equation, where the current decreases with $t^{-1/2}$ as the diffusion layer expands over time. At longer times, the plot exhibits a steady-state region in which the current stabilizes and becomes nearly constant, indicating that the system has reached a dynamic balance due to thin-layer cell effects or persistent surface-controlled processes, such as adsorption or slow kinetics. Furthermore, the current jump observed at ~2000 s may arise from a transient interfacial instability, after which the system regains its structure and displays stable current behaviour.

The Na/2.5C:1M/Na symmetric cells (Fig. 4c), when cycled galvanostatically to study the compatibility with the Na electrode, provide the initial overpotential, $\eta \approx 35$ mV, indicating a stable electrode–electrolyte interface. This overpotential then drops to a negligible value of 2.5 mV and remains stable for 130 h. After this, it slightly increases to ~4 mV for another 100 h, potentially due to small dendrite growth leading to the increase in solid electrolyte interface (SEI) resistance, which may result in a thickening of the SEI layer and voltage fluctuations. This cell exhibits stable stripping/plating for more than 300 h without ohmic losses associated with poor stripping or degradation of the composite polymer electrolyte.[51–54] Fig. S7 shows the Nyquist plot of symmetric 2.5C:1M, having a resistance of 630 Ω cm^{-2}. This shows one diffused semi-circle attributed to charge-transfer resistance and interfacial reactions between the electrolyte and sodium metal.

Open Access Article. Published on 06 March 2026. Downloaded on 6/16/2026 1:20:17 PM.
This article is licensed under a Creative Commons Attribution-NonCommercial 3.0 Unported Licence.

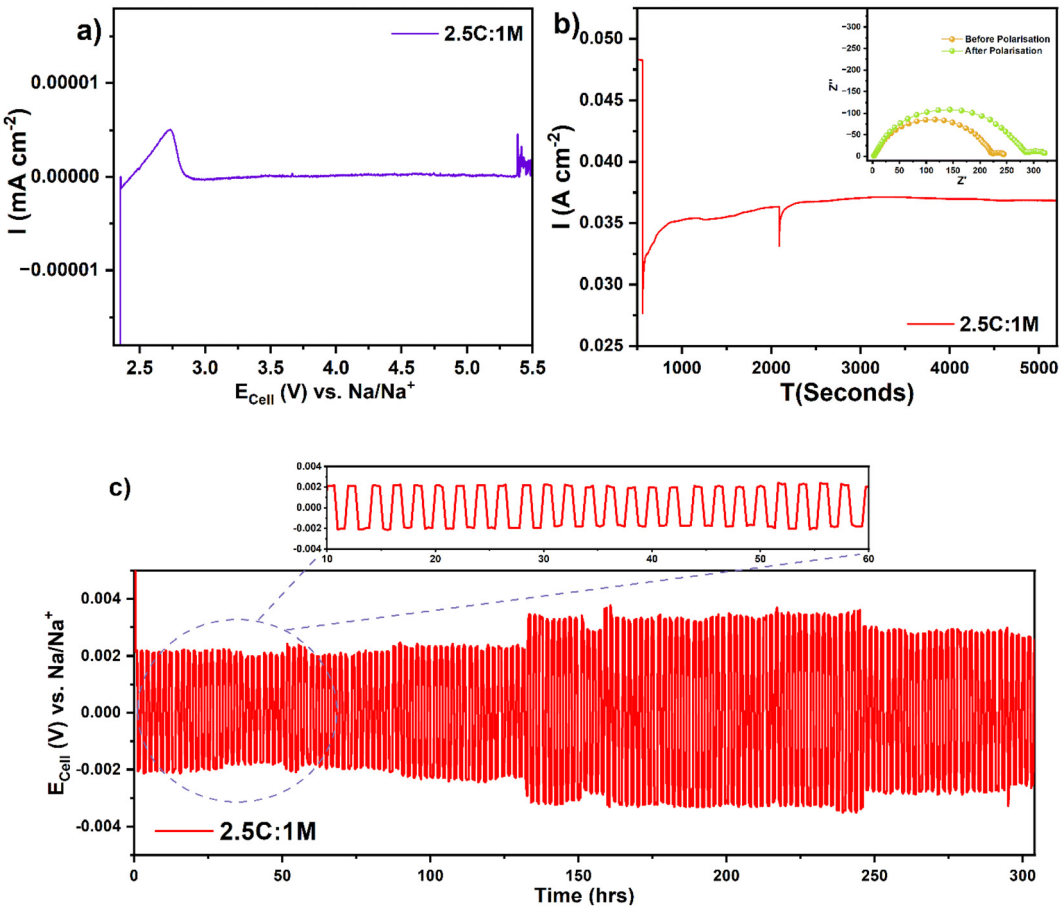

Fig. 4 (a) Linear sweep voltammetry (LSV) plot of the composite polymer electrolyte (CPE) (2.5C:1M) at a scan rate of 0.1 mV s^{-1}. (b) Chronoamperometric plot and (c) stripping/plating of the symmetrical cell (Na/CPE/Na) at a current density of 0.1 mA cm^{-2} with a capacity of 0.1 mA h cm^{-2} (inset-plating behaviour from 10–60 h).

The failed cells were disassembled, and the mechanism of degradation was investigated using several analytical techniques, such as Raman spectroscopy, XPS, and FT-IR spectroscopy, along with electrochemical methods.

4. Post-mortem analysis

Raman and FT-IR spectroscopy are powerful analytical techniques to study molecular vibrations, chemical compositions, and structural properties of materials. In crystalline substances, molecular vibrations can split due to intermolecular interactions within the lattice. By analyzing these split vibrations, interesting changes in properties, such as crystallinity, phase composition, shape, and orientation, can be determined, offering insights into structural variations within composite materials. In order to elucidate the interfacial reactions between the electrolyte and the MoS_2 cathode, *ex situ* FT-IR and Raman spectroscopies were performed. Accordingly, Fig. 5a shows the comparative FT-IR analysis of the cycled symmetric and asymmetric 2.5C:1M cells with pristine composition. The films reveal that the peaks intensified in the range of 1700–1200 cm^{-1}. The OH bending peak at 1638 cm^{-1} broadened and exhibited several new peaks, and at ~3300 cm^{-1}, suggesting interfacial reactions between the Na metal and the electrolyte. Similarly, in Fig. 4b, the OH bending peak at 1638 cm^{-1} for the cycled MoS_2 thin films broadened, and the free OH peak at 3628 cm^{-1} disappeared, while the intramolecular OH peak at 3300 cm^{-1} intensified, revealing the interaction of the MoS_2 with the OH groups of the composite polymer electrolyte. The Si–O stretching peak at 998 cm^{-1} exhibits a slight blue shift to 1005 cm^{-1}, revealing the electronic coupling with MoS_2.[55,56]

Accordingly, Fig. 6a shows the Raman spectra of the comparative cycled symmetric and asymmetric composite polymer electrolyte with the pristine 2.5C:1M. New peaks emerged at 100–400 cm^{-1}, revealing the interaction between the Na metal and the electrolyte. The peaks in this range (144, 187, 214 cm^{-1}) correspond to the O_h symmetry of AlO_6 or MgO_5OH octahedral sheets. The peaks in the range 900–1200 cm^{-1} correspond to the T_d symmetry of the SiO_4 tetrahedral sheets. The peak at 3648 cm^{-1} is assigned to OH vibrations, while the broad envelope below 3600 cm^{-1} (centred at 2676 cm^{-1}) is attributed to OH vibrations in H_2O molecules. These peak intensities have

© 2026 The Author(s). Published by the Royal Society of Chemistry

Open Access Article. Published on 06 March 2026. Downloaded on 6/16/2026 1:20:17 PM.
This article is licensed under a Creative Commons Attribution-NonCommercial 3.0 Unported Licence.

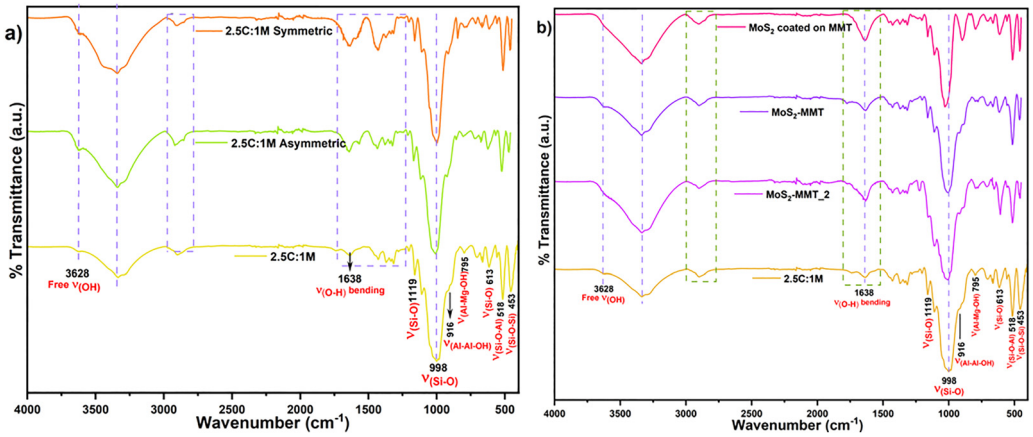

Fig. 5 (a) Comparative FT-IR (post-mortem) analysis of the cycled symmetric and asymmetric 2.5C:1M cells with the fresh composite polymer electrolyte and (b) cycled cells with MoS_2–MMT thin films with the 2.5C:1M electrolyte.

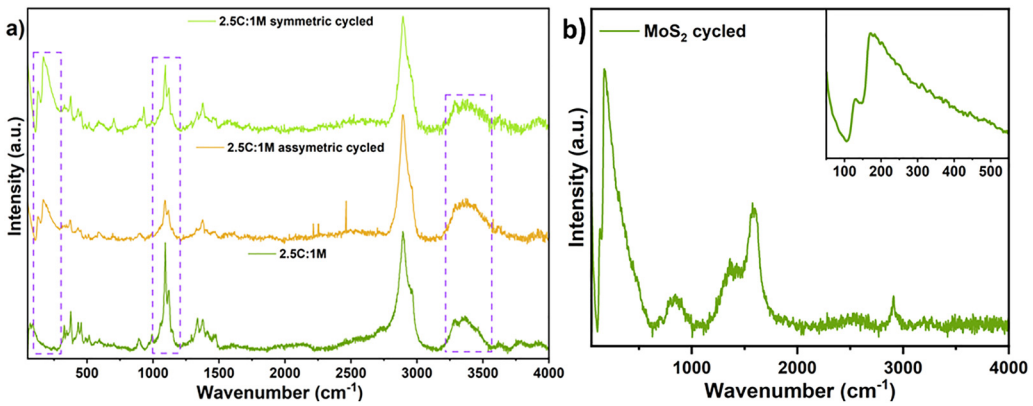

Fig. 6 Comparative Raman post-mortem analysis of the cycled symmetric and asymmetric 2.5C:1M with the fresh composite polymer electrolyte, showing the changes with cycling and (b) cycled MoS_2–MMT thin film.

probably been reduced due to interfacial reactions between the Na metal and the electrolytes.[57–59]

Fig. 6b shows the cycled MoS_2 electrode. The E^1_{2g}, A_{1g} and J_2 bands (centred at ~377, 402 and 222 cm^{-1}, respectively) merged with the O_h symmetry of AlO_6 or MgO_5OH octahedral sheets. Also, several other peaks emerged with cycling, centred around 800, 1300, 1650, and 2900 cm^{-1}, indicating interfacial reactions.

5. Discussions

From the above results, it is evident that exfoliation of MoS_2 results in the formation of few-layered 2D nanosheets with a *d*-spacing of ~0.42 nm, through expansion in the (002) plane and contraction in the (100) plane, respectively, with an additional separation of 5.5–6 Å. Also, the crystallinity is retained after exfoliation of MoS_2, as evident from Raman analysis. The composite polymer electrolyte shows a change in interlayer spacing of 2.08 Å, with the intercalation of CNC nanorods into the 2D MMT nanosheets. This design facilitates Na–ion mobility, as evident from the high transference number of 0.87. Furthermore, we investigated the transference number using pulsed-field gradient NMR spectroscopy. However, due to the higher T_2 relaxation, the diffusion NMR of Na^+ ions was too short to observe. Also, this electrolyte provides an electrochemical stability window of 2.3–5.3 V, which implies this electrolyte could be useful for high voltage cathodes. *Ex situ* analysis reveals the presence of hydroxy groups at the electrode–electrolyte interface, which assists in stable cycling at the anode interface, as evident from galvanostatic cycling with an initial η = 35 mV, and stable stripping/plating for more than 300 h. In contrast, these hydroxy groups could interfere at the cathode–electrolyte interface, which leads to cell failure by altering the crystallinity of MoS_2, as observed by Raman analysis, as the characteristic E^1_{2g} and A_{1g} bands merged.[60–62] More interestingly, distinct changes in the morphology occur, as evident from the SEM images, pointing to the fact that agglomeration takes place in several locations, reducing the high surface area and disrupting the layer-by-layer structure. This is also in complete agreement with data obtained from XPS analysis, suggesting the role of surface oxygen in degradation.

Open Access Article. Published on 06 March 2026. Downloaded on 6/16/2026 1:20:17 PM. This article is licensed under a Creative Commons Attribution-NonCommercial 3.0 Unported Licence.

Incorporation of 2D heterostructures or Janus-type architectures might overcome these issues as an ingenious strategy to achieve more stable electrode interfaces, as the dual-surface chemistry of such materials may facilitate controlled interactions with hydroxyl groups and potentially provide preferential Na–ion transport pathways.[63–65] However, these concepts alone cannot fully resolve the broader interfacial instabilities in solid-state systems. A more comprehensive approach is asymmetric electrolyte engineering, which aims to construct electrolytes capable of forming stable interphases at both anode and cathode sides, as well as across catholyte–anolyte boundaries.[66–68] In theory, multilayer solid electrolytes can integrate complementary functionalities across layers, thereby offsetting individual limitations and producing a Janus-like synergistic behaviour. Nevertheless, the inherent incompatibility between dissimilar electrolyte phases and their interfaces with electrodes remains a central challenge that must be directly addressed rather than assumed to be solved.

To mitigate these issues, asymmetric design strategies attempt to satisfy the distinct electrochemical and mechanical requirements of each electrode by assigning tailored roles to different electrolyte components. Such asymmetry can be introduced at both the macroscale and microscale.

• Macroscale asymmetry involves assembling bi- or multilayer electrolytes composed of disparate materials, typically on the millimetre to centimetre scale, where each layer contributes a specific set of beneficial properties (*e.g.*, mechanical robustness, ionic conductivity, oxidative stability), ably supported by computational modelling and simulations.

• Microscale asymmetry, by contrast, focuses on fine-tuning the chemistry and structure of a single electrolyte phase at the micro- to nano-scale, to generate multifunctional behaviour while avoiding miscibility conflicts, interfacial incompatibility, or excessive interfacial impedance that often arise in macroscale multilayer systems.

Recent studies illustrate the conceptual value of such designs. For example, Tan *et al.* developed an asymmetric fire-retardant quasi-solid polymer electrolyte to address thermal runaway and interfacial instability in lithium metal batteries. A PVDF-HFP gel incorporating organophosphate flame retardants provided enhanced compatibility and thermal stability with high-voltage Ni-rich cathodes, while a polyether gel, synthesized *in situ*, formed a resilient interphase on the lithium metal anode, effectively suppressing dendrite formation.[69] Similarly, Chen *et al.* reported a Zn^{2+}-conductive inorganic SSE based on 2D porphyrin paddlewheel framework MOF sheets; this layer promoted uniform Zn deposition, isolated the metal from bulk aqueous electrolyte, and facilitated $Zn(H_2O)_6^{2+}$ desolvation, resulting in dendrite-free and hydrogen-free cycling. The complementary PAM hydrogel catholyte supplied H^+ carriers and water molecules that acted as lubricants to enable more facile Zn^{2+} insertion/extraction.[70] Zhang *et al.* further demonstrated an asymmetric structural design using a tape-cast polyimide membrane, which provided resistance to lithium dendrite formation while maintaining compatibility with high-voltage cathodes.[71]

Together, these studies suggest that, while asymmetric electrolyte architecture is a promising framework, its success relies not merely on assembling multiple layers, but on rationally assigning distinct structural and chemical roles to each component. The approach must still contend with unresolved challenges, including phase compatibility, mechanical integrity, and long-term interfacial stability, before it can be considered as a broadly applicable strategy for next-generation solid-state batteries.

6. Conclusions

The CNC–MMT composite polymer electrolyte shows enhanced interfacial stability with Na metal, revealing an initial overpotential of (η) 35 mV, inferring the formation of a stable electrode–electrolyte interface. This also shows a wide electrochemical stability window of 2.3–5.3 V with a high transference number of $\sim$0.87. FT-IR and Raman spectroscopic analyses provide important clues to understanding the interfacial chemistry, since a pronounced hydroxyl stretching band is observed, attributed to the CNC component of the electrolyte. Furthermore, XPS and EDX analyses verify the presence of surface oxygen. In contrast, this hydroxyl functionality appears to disrupt interfacial stability at the cathode, as the E^1_{2g} and A_{1g} bands have merged, reducing the crystallinity and potentially contributing to cell failure during extended cycling. However, it simultaneously facilitates enhanced sodium–ion mobility at the anode interface, with stable cycling for more than 300 h; likely by promoting favourable ion coordination with sodium metal. This dual behaviour highlights the complex interplay between electrolyte chemistry and electrode interfaces, underscoring the need for precise functional group tuning in future electrolyte designs.

Conflicts of interest

The authors declare no competing financial interest.

Data availability

All the data supporting the findings of this study are fully available within the article. No additional datasets were generated or analysed beyond those reported in this manuscript.

Supplementary information (SI) is available. See DOI: https://doi.org/10.1039/d6ya00014b.

Acknowledgements

R. K. P. acknowledges the Department of Science and Technology for an INSPIRE Faculty Award Grant [DST/INSPIRE/04/2016/002370] and the Core Research Grants [CRG/2020/006281 and CRG/2021/004759] from ANRF, Government of India. V. K. P. would like to thank the SERB for the J. C. Bose Fellowship (JCB/2020/000018). S. M. thanks the SAIF, IIT Bombay, for the HR-TEM measurements. C. T. acknowledges support from the

© 2026 The Author(s). Published by the Royal Society of Chemistry

Open Access Article. Published on 06 March 2026. Downloaded on 6/16/2026 1:20:17 PM. This article is licensed under a Creative Commons Attribution-NonCommercial 3.0 Unported Licence.

Department of Science and Technology, Government of India, for the INSPIRE fellowship.

References

1 A. M. Bates, Y. Preger, L. Torres-Castro, K. L. Harrison, S. J. Harris and J. Hewson, Are solid-state batteries safer than lithium-ion batteries?, *Joule*, 2022, **6**, 1–14.
2 Y. S. Meng, V. Srinivasan and K. Xu, Designing better electrolytes, *Science*, 2022, **378**, eabq3750.
3 J. Janek and W. G. Zeier, A solid future for battery development, *Nat. Energy*, 2016, **1**, 16141.
4 S. Randau, D. A. Weber, O. Kötz, R. Koerver, P. Braun, A. W. E. Ivers-Tiffée, T. Adermann, J. Kulisch, W. G. Zeier, F. H. Richter and J. Janek, Benchmarking the performance of all-solid-state lithium batteries, *Nat. Energy*, 2020, **5**, 259–270.
5 T. Famprikis, P. Canepa, J. A. Dawson, M. S. Islam and C. Masquelier, Fundamentals of inorganic solid-state electrolytes for batteries, *Nat. Mater.*, 2019, **18**, 1278–1291.
6 E. P. Roth and C. J. Orendorff, How Electrolytes Influence Battery Safety, *Electrochem. Soc. Interface*, 2012, **21**, 45–49.
7 Q. Zhao, S. Stalin, C.-Z. Zhao and L. A. Archer, Designing solid-state electrolytes for safe, energy-dense batteries, *Nat. Rev. Mater.*, 2020, **5**, 229–252.
8 Y. Choo, D. M. Halat, I. Villaluenga, K. Timachova and N. P. Balsara, Diffusion and migration in polymer electrolytes, *Prog. Polym. Sci.*, 2020, **103**, 101220.
9 J. V. L. Mota, M. Albuquerque, D. Brandell and L. T. Costa, Exploring structural and dynamical properties of polymer-ionic liquid ternary electrolytes for sodium ion batteries, *Electrochim. Acta*, 2023, **461**, 142635.
10 C. Hansel, E. Lizundia and D. Kundu, A Single Li-Ion Conductor Based on Cellulose, *ACS Appl. Energy Mater.*, 2019, **2**, 5686–5691.
11 S. Mandal, V. K. Pillai, M. R. Ponraj, K. M. Thushara, J. Bhagavathsingh, S. L. Grage, J. W. Kang, X. Peng, A. N. M. Kannan, D. Liepmann, V. Thavasi and V. Renugopalakrishnan, van der Waals gap modulation of graphene oxide through mono-Boc ethylenediamine anchoring for Li-ion batteries, *Energy Adv.*, 2024, **3**, 1977–1991.
12 D. K. Chouhan, T. U. Patro, G. Harikrishnan, S. Kumar, S. Gupta, G. S. Kumar, H. Cohen and H. D. Wagner, Graphene oxide-Laponite hybrid from highly stable aqueous dispersion, *Appl. Clay Sci.*, 2016, **132–133**, 105–113.
13 V. Vijayakumar, M. Ghosh, K. Asokan, S. B. Sukumaran, S. Kurungot, J. Mindemark, D. Brandell, M. Winter and J. R. Nair, 2D Layered Nanomaterials as Fillers in Polymer Composite Electrolytes for Lithium Batteries, *Adv. Energy Mater.*, 2023, **13**, 2203326.
14 J. Shim, H. J. Kim, B. G. Kim, Y. S. Kim, D. G. Kim and J. C. Lee, 2D Boron Nitride Nanoflakes as A Multifunctional Additive in Gel Polymer Electrolytes for Safe, Long Cycle Life and High Rate Lithium Metal Batteries, *Energy Environ. Sci.*, 2017, **10**, 1911–1916.
15 P. B. Zhai, Z. L. Yang, Y. Wei, X. X. Guo and Y. J. Gong, Two-Dimensional Fluorinated Graphene Reinforced Solid Polymer Electrolytes for High-Performance Solid-State Lithium Batteries, *Adv. Energy Mater.*, 2022, **12**, 2200967.
16 Q. Pan, Y. Zheng, S. Kota, W. Huang, S. Wang, H. Qi, S. Kim, Y. Tu, M. W. Barsoum and C. Y. Li, 2D MXene-Containing Polymer Electrolytes for All-Solid-State Lithium Metal Batteries, *Nanoscale Adv.*, 2019, **1**, 395–402.
17 T. Subhani, S. Khademolqorani, S. N. Banitaba, M. Ramadan, A. Khaliq, I. A. Chaudhry and A. I. Osman, Advancements in Battery Materials: Bio-Based and Mineral Fillers for Next-Generation Solid Polymer Electrolytes, *ACS Appl. Mater. Interfaces*, 2024, **16**, 63089–63108.
18 S. Maiti, A. Pramanik, S. Chattopadhyay, G. De and S. Mahanty, Electrochemical energy storage in montmorillonite K10 clay based composite as supercapacitor using ionic liquid electrolyte, *J. Colloid Interface Sci.*, 2015, **464**, 73–82.
19 Y. Ma, L. B. Li, G. X. Gao, X. Y. Yang and Y. You, Effect of montmorillonite on the ionic conductivity and electrochemical properties of a composite solid polymer electrolyte based on polyvinylidenedifluoride/polyvinyl alcohol matrix for lithium ion batteries, *Electrochim. Acta*, 2016, **187**, 535–542.
20 M. Deka and A. Kumar, Electrical and electrochemical studies of poly(vinylidene fluoride)–clay nanocomposite gel polymer electrolytes for Li-ion batteries, *J. Power Sources*, 2011, **196**, 1358–1364.
21 L. Wu, X. He, Y. Zhao, K. Huang, Z. Tong, B. Liao and H. Pang, Montmorillonite-based materials for electrochemical energy storage, *Green Chem.*, 2024, **26**, 678–704.
22 C. He, J. Liu, J. Cui, J. Li and X. Wu, A gel polymer electrolyte based on Polyacrylonitrile/organic montmorillonite membrane exhibiting dense structure for lithium-ion battery, *Solid State Ionics*, 2018, **315**, 102–110.
23 S. Kim, E.-J. Hwang, Y. Jung, M. Han and S.-J. Park, Ionic conductivity of polymeric nanocomposite electrolytes based on poly(ethylene oxide) and organo-clay materials, *Colloids Surf., A*, 2008, **313–314**, 216–219.
24 Y. Zhao and Y. Wang, Tailored Solid Polymer Electrolytes by Montmorillonite with High Ionic Conductivity for Lithium-Ion Batteries, *Nanoscale Res. Lett.*, 2019, **14**, 366.
25 P. Dhatarwal, R. J. Sengwa and S. Choudhary, Effectively improved ionic conductivity of montmorillonite clay nanoplatelets incorporated nanocomposite solid polymer electrolytes for lithium ion-conducting devices, *SN Appl. Sci.*, 2019, **1**, 112.
26 H. Chen, C. Kang, E. Shang, G. Liu, D. Chen and Z. Yuan, Montmorillonite-Based Separator Enables a Long-Life Alkaline Zinc−Iron Flow Battery, *Ind. Eng. Chem. Res.*, 2023, **62**, 676–684.
27 S. Mandal, C. Tom, Y. Singh, H. Khoder, P. Launois, E. Paineau, S. L. Grage, M. Schaller, S. Alwarappan, R. S. Singh, R. K. Pujala and V. K. Pillai, Domain Size Modulation of Clay−Nanocellulose Composites for Enhanced Na-Ion Transport, *ACS Appl. Energy Mater.*, 2025, **8**(9), 6071–6086, DOI: 10.1021/acsaem.5c00452.

© 2026 The Author(s). Published by the Royal Society of Chemistry

Open Access Article. Published on 06 March 2026. Downloaded on 6/16/2026 1:20:17 PM. This article is licensed under a Creative Commons Attribution-NonCommercial 3.0 Unported Licence.

28 S. Mandal, C. Tom, S. Alwarappan, R. K. Pujala, S. K. Martha and V. K. Pillai, Understanding Interfacial Reactions and Electrochemical Performance of MoS_2 Cathodes with Laponite-Based Solid Polymer Electrolytes, *Solid State Ionics*, 2025, **423**, 117052.

29 X. Zhang, H. Yi, H. Bai, Y. Zhao, F. Min and S. Song, Correlation of montmorillonite exfoliation with interlayer cations in the preparation of two dimensional nanosheets, *RSC Adv.*, 2017, **7**, 41471–41478.

30 A. K. Sonker, S. Xiong, R. Aggarwal, M. Olsson, A. Spule, S. Hosseini, S. K. Sonkar, A. Matic and G. Westman, Exfoliated MoS_2 Nanosheet/Cellulose Nanocrystal Flexible Composite Films as Electrodes for Zinc Batteries, *ACS Appl. Nano Mater.*, 2023, **6**, 8270–8278.

31 M. Acerce, D. Voiry and M. Chhowalla, Metallic 1T phase MoS_2 nanosheets as supercapacitor electrode materials, *Nat. Nanotechnol.*, 2015, **10**, 313–318.

32 B. Li, X. Liang, G. Li, F. Shao, T. Xia, S. Xu, N. Hu, Y. Su, Z. Yang and Y. Zhang, Inkjet-Printed Ultrathin MoS_2-Based Electrodes for Flexible In-Plane Microsupercapacitors, *ACS Appl. Mater. Interfaces*, 2020, **12**, 39444–39454.

33 J. Heising and M. G. Kanatzidis, Exfoliated and Restacked MoS_2 and WS_2: Ionic or Neutral Species? Encapsulation and Ordering of Hard Electropositive Cations, *J. Am. Chem. Soc.*, 1999, **121**, 11720–11732.

34 Y. Hong, J. Lim, J. Min, N. Agarwal, R. Hovden, A. Bol and Y. Li, Delayed 1T to 2H Phase Transition Upon Electrochemical Delithiation of $LiMoS_2$, *Phys. Rev. Mater.*, 2026, **10**, 014002.

35 H. Li, Q. Zhang, C. C. R. Yap, B. K. Tay, T. H. T. Edwin, A. Olivier and D. Baillargeat, From Bulk to Monolayer MoS_2: Evolution of Raman Scattering, *Adv. Funct. Mater.*, 2012, **22**, 1385–1390.

36 G. L. Frey, R. Tenne, M. J. Matthews, M. S. Dresselhaus and G. Dresselhaus, Raman and resonance Raman investigation of MoS_2 nanoparticles, *Phy. Rev. B: Condens. Matter Mater. Phys.*, 1999, **60**(4), 2883–2892.

37 T. Xie and P. Sun, Electrochemical performance of interspace-expanded molybdenum disulfide few-layer, *J. Nanopart. Res.*, 2018, **20**, 183.

38 R. T. Sam, T. Umakoshi and P. Verma, Probing stacking configurations in a few layered MoS_2 by low frequency Raman spectroscopy, *Sci. Rep.*, 2020, **10**, 21227.

39 L. Yang, X. Cui, J. Zhang, K. Wang, M. Shen, S. Zeng, S. A. Dayeh, L. Feng and B. Xiang, Lattice strain effects on the optical properties of MoS_2 nanosheets, *Sci. Rep.*, 2014, **4**, 5649.

40 L. Jianga, S. Zhang, S. A. Kulinich, X. Song, X. Zhu, X. Wang and H. Zeng, Optimizing Hybridization of 1T and 2H Phases in MoS_2 Monolayers to Improve Capacitances of Supercapacitors, *Mater. Res. Lett.*, 2015, **3**(4), 177–183.

41 D. Gopalakrishnan, D. Damien and M. M. Shaijumon, MoS_2 Quantum Dot-Interspersed Exfoliated MoS_2 Nanosheets, *ACS Nano*, 2014, **5**(8), 5297–5303.

42 Y. Ge, R. Jalili, C. Wang, T. Zheng, Y. Chao and G. G. Wallace, A robust free-standing MoS_2/poly(3,4-ethylenedioxythiophene):poly (styrenesulfonate) film for supercapacitor applications, *Electrochim. Acta*, 2017, **235**, 348–355.

43 Y. Zhu, H. Li, Y. Wu, L. Yang, Y. Sun, G. Chen, Y. Liu, Z. Wu, C. Zhang and X. Guo, Unveiling the abnormal capacity rising mechanism of MoS_2 anode during long-term cycling for sodium-ion batteries, *RSC Adv.*, 2021, **11**(46), 28488–28495, DOI: 10.1039/d1ra05518f.

44 Q. Lin, X. Dong and Y. Wang, *et al.*, Molybdenum disulfide with enlarged interlayer spacing decorated on reduced graphene oxide for efficient electrocatalytic hydrogen evolution, *J. Mater. Sci.*, 2020, **55**, 6637–6647, DOI: 10.1007/s10853-020-04478-w.

45 G. Eda, T. Fujita, H. Yamaguchi, D. Voiry, M. W. Chen and M. Chhowalla, Coherent atomic and electronic heterostructures of single-layer MoS_2, *ACS Nano*, 2012, **6**, 7311–7317.

46 H. S. S. Matte, MoS_2 and WS_2 analogues of graphene, *Angew. Chem., Int. Ed.*, 2010, **49**, 4059–4062.

47 R. A. Gordon, D. Yang, E. D. Crozier, D. T. Jiang and R. F. Frindt, Structures of exfoliated single layers of WS_2, MoS_2, and $MoSe_2$ in aqueous suspension, *Phys. Rev. B: Condens. Matter Mater. Phys.*, 2003, **65**, 125407.

48 J. Evans, C. A. Vincent and P. G. Bruce, Electrochemical measurement of transference numbers in polymer electrolytes, *Polymer*, 1987, **28**(13), 2324–2328.

49 C. A. Vincent and P. G. Bruce, Effect of Ion Association on Transport in Polymer Electrolytes, *Faraday Discuss. Chem. Soc.*, 1989, **88**, 43–54.

50 M. Watanabe, S. Nagano, K. Sanui and N. Ogata, Estimation of Li^+ Transport Number in Polymer Electrolytes by the Combination of Complex Impedance and Potentiostatic Polarization Measurements, *Solid State Ionics*, 1988, **28–30**, 911–917.

51 W. Sun, Y. Li, C. Sun, X. Yuan, H. Jin and Y. Zhao, Deciphering the electrochemical-mechanical coupling failure mechanism of Na-NASICON solid-state batteries, *Mater. Futures*, 2025, **4**, 035102.

52 A. Mills, S. Kalnaus, W.-Y. Tsai, Y.-F. Su, E. Williams, X. Zheng, S. Vaidyanathan, D. T. Hallinan Jr., J. Nanda and G. Yang, Elucidating Polymer Binder Entanglement in Freestanding Sulfide Solid-State Electrolyte Membranes, *ACS Energy Lett.*, 2024, **9**, 2677–2684.

53 Y. Ji, J. Qiu, W. Zhao, T. Liu, Z. Dong, K. Yang, G. Zheng, G. Qian, M. Yang, Q. Chen, K. Amine, F. Pan and L. Yang, *In situ* probing the origin of interfacial instability of Na metal anode, *Chem*, 2023, **9**, 2943–2955.

54 J. H. Um and S. H. Yu, Unraveling the Mechanisms of Lithium Metal Plating/Stripping *via in situ*/*operando* Analytical Techniques, *Adv. Energy Mater.*, 2021, **11**(27), 2003004, DOI: 10.1002/aenm.202003004.

55 V. C. Farmer and J. D. Russell, The infra-red spectra of layer silicates, *Spectrochim. Acta*, 1964, **20**, 1149–1173.

56 M. Pelletier, L. J. Michot, B. Humbert, O. Barrès, J.-B. D'Espinose de la Caillerie and J.-L. Robert, Influence of layer charge on the hydroxyl stretching of trioctahedral clay

 © 2026 The Author(s). Published by the Royal Society of Chemistry

Open Access Article. Published on 06 March 2026. Downloaded on 6/16/2026 1:20:17 PM.
This article is licensed under a Creative Commons Attribution-NonCommercial 3.0 Unported Licence.

minerals: a vibrational study of synthetic Na- and K-saponites, *Am. Mineral.*, 2003, **88**, 1801–1808.

57 A. Wang, J. J. Freeman and B. L. Jolliff, Understanding the Raman spectral features of phyllosilicates, *J. Raman Spectrosc.*, 2015, **46**, 829–845.

58 M. Ritz, L. Vaculíková, J. Kupková, E. Plevová and L. Bartonová, Different level of fluorescence in Raman spectra of montmorillonites, *Vib. Spectrosc.*, 2016, **84**, 7–15.

59 N. P. N. Wellala, A. M. Hollas, K. Duanmu, V. Murugesan, X. Zhang, R. Feng, Y. Shao and W. Wang, Decomposition pathways and mitigation strategies for highly-stable hydroxyphenazine flow battery anolytes, *J. Mater. Chem. A*, 2021, **9**, 21918–21928.

60 Y. Li, C. Sun, Z. Sun, M. Li, H. Jin and Y. Zhao, Boosting Na–O Affinity in $Na_3Zr_2Si_2PO_{12}$ Electrolyte Promises Highly Rechargeable Solid-State Sodium Batteries, *Adv. Funct. Mater.*, 2024, **34**(40), 2403937.

61 C. Sun, Y. Li, Z. Sun, X. Yuan, H. Jin and Y. Zhao, Ferroelectric interface for efficient sodium metal cycling in anode-free solid-state batteries, *Mater. Today*, 2024, **80**, 395–405, DOI: 10.1016/j.mattod.2024.09.018.

62 C. Wang, J. Gao, X. Gao and Y. Zhao, Stabilizing the Na/$Na_3Zr_2Si_2PO_{12}$ interface through intrinsic feature regulation of $Na_3Zr_2Si_2PO_{12}$, *Cell Rep. Phys. Sci.*, 2021, **2**, 100478.

63 E. Pomerantseva and Y. Gogotsi, Two-dimensional heterostructures for energy storage, *Nat. Energy*, 2017, **2**, 17089, DOI: 10.1038/nenergy.2017.89.

64 J. Sun, M. Sadd, P. Edenborg, H. Grönbeck, P. H. Thiesen, Z. Xia, V. Quintano, R. Qiu, A. Matic and V. Palermo, Real-time imaging of Na^+ reversible intercalation in "Janus" graphene stacks for battery applications, *Sci. Adv.*, 2021, **7**, eabf0812.

65 Y. Li, Z. Wang, C. Sun, S. Q. Liu, Y. Dou, X. Yuan, H. Jin and Y. Zhao, Na-K Interlayer Driven Na-NASICON Solid-State Batteries, *Adv. Funct. Mater.*, 2025, **35**(27), 2425995.

66 S. Chen and C. Zhi, Design of asymmetric electrolytes for aqueous zinc batteries, *Commun. Chem.*, 2025, **8**, 20, DOI: 10.1038/s42004-024-01405-x.

67 Y. Zhang, C. Tang and R. Gu, *et al.*, Batteries with asymmetric solid-state electrolytes for sustainable energy storage, *Nano Res.*, 2025, **18**(5), 94907316, DOI: 10.26599/NR.2025.94907316.

68 X. Yu and A. Manthiram, Electrode–Electrolyte Interfaces in Lithium–Sulfur Batteries with Liquid or Inorganic Solid Electrolytes, *Acc. Chem. Res.*, 2017, **50**(11), 2653–2660, DOI: 10.1021/acs.accounts.7b00460.

69 S. J. Tan, J. Yue, Z. Chen, X. X. Feng, J. Zhang, Y. X. Yin, L. Zhang, J. C. Zheng, Y. Luo and S. Xin, *et al.*, Asymmetric Fire-Retardant Quasi Solid Electrolytes for Safe and Stable High-Voltage Lithium Metal Battery, *Energy Mater. Adv.*, 2024, **5**, 0076, DOI: 10.34133/energymatadv.0076.

70 S. Chen, Y. Ying and L. Ma, *et al.*, An asymmetric electrolyte to simultaneously meet contradictory requirements of anode and cathode, *Nat. Commun.*, 2023, **14**, 2925, DOI: 10.1038/s41467-023-38492-8.

71 Z. Zhang, W. Fan, K. Cui, J. Gou and Y. Huang, Design of Ultrathin Asymmetric Composite Electrolytes for Interfacial Stable Solid-State Lithium-Metal Batteries, *ACS Nano*, 2024, **18**(27), 17890–17900, DOI: 10.1021/acsnano.4c04429.